Accepted Article

Title: Enhanced Catalytic Properties of Molybdenum Promoted Mesoporous Cobalt Oxide: Structure-Surface-Dependent Activity for Selective Synthesis of 2-Substituted Benzimidazoles

Authors: Chandima Weerakkody, Dinithi Rathnayake, Junkai He He, Biswanath Dutta, Peter Kerns, Laura Achola, and Steve L. Suib

Enhanced Catalytic Properties of Molybdenum Promoted Mesoporous Cobalt Oxide: Structure-Surface-Dependent Activity for Selective Synthesis of 2-Substituted Benzimidazoles

Chandima Weerakkody, Dinithi Rathnayake, Junkai He, Biswanath Dutta, Peter Kerns, Laura Achola, Steven L. Suib[*]

Department of Chemistry and Institute of Materials Science, University of Connecticut, 55 North Eagleville Road, U-3060, Storrs, CT 06269, United States

Abstract

High-valent molybdenum ions were substituted into the cobalt oxide lattice through a one step, sol-gel method and investigated for selective synthesis of 2-substituted benzimidazoles. Catalyst synthesis involves surfactant assisted soft templating inverse micelle method, which forms mesopores by interconnected intraparticle voids. Substitutional doping of Mo^{6+} resulted in materials with modified structural, morphological, surface, and redox properties. The catalytic activity increased with Mo concentration until an optimum amount (3 % Mo incorporation). Modified material shows lattice expansion, increased surface oxygen vacancies, and high surface area, which are responsible for the higher catalytic activity in selective benzimidazole synthesis reaction. A strong correlation between surface properties of the catalyst and the product selectivity was observed and plausible mechanistic and kinetic data are proposed and collected, respectively.

1

1. Introduction

Benzimidazole derivatives exhibit a broad spectrum of pharmacological and biological applications in clinical medicines and bioactive compounds.[1] Recently reported pharmacological products containing benzimidazole rings have been used to treat diseases such as ischemia-reperfusion injury, hypertension, and obesity. In addition, benzimidazole derivatives have been reported as antivirus, antibacterial, and antiparasitic agents as well as inhibitors of the hepatitis C virus, RNA polymerase, and angiotensin.[2] Due to the growing interest of these compounds in the field of drug development and the pharmaceutical industry, a number of synthetic protocols have been introduced recently. They include palladium catalyzed tandem carbonylation cyclization reactions of o-phenylenediamine[3], palladium catalyzed tandem dehydration-coupling reactions of 2-bromoaniline[4], reductive cyclization reactions of o-nitroaniline with aldehydes[5], cyclization of o-phenylenediamines by CO_2 in the presence of H_2[4], trimethylsilyl chloride promoted reactions of o-phenylenediamine and aldehyde[1], and condensation of o-phenylenediamines and carboxylic acids[6]. Among these systems, the condensation reaction of o-phenylenediamines and aldehydes under oxidative condition turned out to be the most facile method to synthesize 2-substituted and 1,2-disubstituted benzimiazole derivatives. This method is preferred in terms of applications as a wide range of 2-substituted benzimidazole derivatives could be obtained due to the availability of a high variety of aldehydes.[7] However, these reactions require either stoichiometric amounts of hydrogen acceptors or strong bases in order to achieve efficient and selective benzimidazole yields, which has been an issue of high interest.[8–10]

2

An alternative protocol is the one-pot tandem synthesis from amines in the presence of a bifunctional catalyst, where amines are in situ oxidized to aldehydes followed by cyclocondensation with amine compounds. Different oxide based heterogeneous catalytic systems have been explored for the synthesis of benzimidazole derivatives including alluminosilicates, iron oxide, cobalt oxide, zinc oxide, copper oxide, and molybdenum oxide. However, lower yields of 2-benzimidazole have emerged as a major concern due to the formation of 1,2-disubstituted derivatives as by-products. Zhang et al. reported Lewis acidity of the catalyst plays a crucial role for the selective synthesis of of 2-substituted benzimidazoles by evaluating catalytic activity of different acid catalysts including $ZrCl_4$, $HfCl_4$, $SnCl_4$, and $InBr_3$.[2] Various other metal salts such as $Mg(ClO_4)_2$, $NH_4Ce(NO_3)_2$, and LiBr showed either lower selectivity or no activity.[2] Similarly, MoO_3-SiO_2 has been used as bifunctional catalysts for selective synthesis of 2-benzimidazoles in the presence of H_2O_2.[11] MoO_3 incorporated ZrO_2 exhibits strong solid acidity and excellent catalytic activity for use in organic transformation reactions.[12,13]

Considerable progress has been made employing complexes of base metals (Fe, Co, Mn, Ni) in various dehydrogenation reactions.[14] Cobalt catalysts have been reported in hydrogenation reactions of olefins, ketones, imines, and CO_2.[15–18] Co_3O_4 has emerged as an interesting catalytic material and has gained much attention due to superior oxygen storage/release and redox properties due to the multivalent nature.[19] Mesoporous materials possess high surface areas and large pore volumes, which provide more accessible active sites and facilitate diffusion of reactants and products, for efficient and enhanced catalytic performance compared to their non porous counterparts.[20,21]

In the process of developing low loading, environmentally sound, affordable, stable and

3

selective meal oxide catalysts for greener organic reactions, we report mesoporous cobalt oxide as a mild oxidation catalyst which can be further modified to achieve bifunctional catalytic effects for the synthesis of 2-benzimidazoles. Synthesis procedures for mesoporous Co_3O_4 involve sol-gel processes where inverse surfactant micelles act as soft templates for the mesopores.[22] Moreover, the use of molybdenum as a promoter to adjust the acidic strength of cobalt oxide was explored for the selective synthesis of 2-substituted benzimidazole derivatives. Effects of the incorporation of molybdenum cation into the Co_3O_4 unit cell were further explored by evaluating chemical and morphological characteristics, and the catalytic activity of the material.

2. Experimental

2.1. Catalyst preparation

Mesoporous cobalt oxide was synthesized by dissolving 5 g (0.027 mol) of $Co(NO_3)_2 \cdot 6H_2O$ in a solution containing 34 g (0.66 mol) of 1-butanol, 2.4 g (0.038 mol) of HNO_3, and 2.5 g (4.31 x 10^{-4} mol) of P123. The resulted mixture was heated at 120 °C for 5 hours and the formed solid was calcined at 150 °C for 12 hours. The obtained powder was calcined at 300 °C for 4 hours to get the crystalline mesoporous Co_3O_4. To prepare the Mo promoted Co_3O_4, certain amounts of $(NH_4)_6Mo_7O_{24}.4H_2O$ were dissolved in a minimum amount of water and added to the initial mixture according to the metal loading ratio and all the other steps are similar to the procedure described above. The metal dopant amounts were 1, 3, and 5 mol % with respect to the total metal precursors. The samples were labeled as X%Mo-Co_3O_4, where X is 1, 3, or 5 standing for the molar percentage of molybdenum loading in Co_3O_4.

4

2.2. Catalyst characterization

Powder X-ray diffraction (PXRD) data were collected ($2\theta = 5$-$75°$) using a Rigaku Ultima IV diffractometer with Cu Kα radiation ($\lambda = 1.5406$ Å) at an operating voltage of 40 kV and a beam current of 44 mA. N_2 sorption analysis was performed on a Quantachrome Autosorb-1-1C automated sorption system. The samples were degassed at 150 °C for 4 h prior to each measurement to remove physically adsorbed species. The surface areas were obtained by the Brunauer-Emmett-Teller (BET) method, and the pore size distributions were calculated by the Barrett-Joyner-Halenda (BJH) method using the desorption data.

To measure the acid/base character of synthesized materials, CO_2 sorption experiments were performed on the Quantachrome Autosorb-1-1C automated adsorption system. All samples were heated under vacuum at 150 ˚C for 6 h prior to experiments. The adsorption studies of all materials were done at room temperature (25 ˚C). A water circulating bath was used to control the temperature.

Morphological characterization was examined with a Zeiss DSM 982 Gemini field-emission scanning electron microscope (FE-SEM) with a Schottky emitter at an accelerating voltage of 2.0 kV. Elemental mapping of the materials was carried out on an Oxford AZtec Energy microanalysis system equipped with an X-Max 80 silicon drift detector. High-resolution transmission electron microscopy (HR-TEM) images were collected by a JEOL 2010 FasTEM microscope operating at 200 kV with an energy dispersive X-ray spectroscopy (EDS) detector. The samples were dispersed in ethanol and mounted on a copper grid coated with carbon film. X-ray Photoelectron

5

Spectroscopy (XPS) measurements were carried out on a PHI model 590 spectrometer with multi probes (ΦPhysical Electronics Industries Inc.), using Al Kα radiation ($\lambda =$ 1486.6 eV) as the radiation source. The binding energies reported in this study were corrected for specimen charging by referencing them to the C 1s peak (set at 284.6 eV). Raman measurements were performed on a Renishaw 2000 Raman microscope attached to a charge-coupled device (CCD) camera with an Ar^+ laser at 514.4 nm as the excitation source and the instrument was calibrated using a silicon wafer as the reference.

Temperature-programmed mass spectrometry analyses were conducted in a programmable tube furnace equipped with a gas analyzer MKS coupled with a quadruple mass selective detector. About 50 mg of materials were packed in a quartz tube reactor mounted into the tube furnace. The loaded samples were pretreated in an inert gas flow (Ar) at 150 °C for 1 h to clean the catalyst surface before each test. For H_2-TPR measurements, 5% H_2/ Ar flow was passed through the catalyst bed at a flow rate of 50 sccm, while the temperature was ramped from room temperature (RT) to 800 °C with a heating ramp rate of 10 °C/min.

2.3. Catalytic activity measurements

In a typical reaction, benzylamine (0.6 mmol), o-phenylenediamine (0.5 mmol), meso Mo-Co_3O_4, and 1-butanol (1 mL) were placed in a 25 mL round-bottom flask (two-necked flask for time- dependence studies, where the second neck was used as a sample port). The flask containing the reaction mixture with a reflux condenser attached was immersed in a silicone oil bath preheated to 100 °C. The reaction mixture was refluxed with constant stirring (500 rpm) for the required time under atmospheric air. After the

6

reaction, the mixture was cooled, the catalyst was removed by filtration, and the filtrate

was analyzed by gas chromatography-mass spectroscopy (GC-MS) methods using a

7820A GC system connected with a thermal conductivity detector of 5975 series MSD

from Agilent Technologies. A nonpolar cross-linked methyl siloxane column with

dimensions of 12 in $\times$ 0.200 mm $\times$ 0.33 m was used. For recycle experiments, the catalyst

was separated by filtration at the end of the reaction, washed several times with ethanol,

and heated in the oven at 250 °C for one hour.

3. Results

3.1. Physicochemical properties

3.1.1. PXRD and TEM

Figure 1(a) shows wide angle PXRD patterns for pure Co_3O_4 and Mo promoted Co_3O_4

with different Mo loading amounts. Up to 3% Mo loaded Co_3O_4 materials show similar

XRD patterns, which represent the typical Co_3O_4 spinel crystal structure (JCPDS #

090418). 3%Mo-Co calcined at 150 °C shows a mixture containing Co_3O_4 and

$C_4H_6CoO_4 \cdot 4H_2O$ indicating the incomplete transformation of the material into Co_3O_4,

which is consistent with the data reported in literature (**Figure S1**).[23] In 5%Mo-Co_3O_4

material a small peak appears around 26°, which can be indexed to the cobalt molybdate

($CoMoO_4$) crystal phase. For comparison, pure $CoMoO_4$ was synthesized and the PXRD

of $CoMoO_4$ matches the peaks in 5%Mo- Co_3O_4 PXRD. The average crystallite size was

calculated using the Scherrer equation ($\tau = K\lambda / B \cos \theta$ where τ = crystallite size, K =

shape factor, λ = x-ray wavelength, and B = line broadening at half maximum). A trend

of crystallite size decreasing with dopant amounts up to 3%Mo loadings was observed

7

and the 5% material has a crystallite size close to pure Co_3O_4 (**Figure 4).** Crystallite size

of these materials are in the range of 11.2 to 14.7 nm and the largest size was observed

for bare Co_3O_4 material.

The change of nanoparticle sizes upon the Mo loading was also observed in TEM

analyses and all the materials exhibited crystalline walls with well defined lattice fringes

(**Figure 3**). All TEM images were taken with the same magnification for better

evaluation of the change of the particle sizes and each particle was composed of

nanoparticle aggregates. With the dopant amount increasing from 0% to 3%, a decrease

in particle size was observed and all the materials showed uniform pore structure. In HR-

TEM the d spacings were calculated as 0.25 nm and 0.48 nm for (311) and (111) planes,

respectively (**Figure 3(e)**).

3.1.2. N_2 and CO_2 sorption studies

Barrett-Joyner-Halenda (BJH) desorption pore diameters decreased with the introduction

of Mo into Co_3O_4 (**Figure 1(c)**). Pure cobalt oxide has a pore diameter of 20 nm and this

decreased to 15.5 nm in the 3%Mo-Co_3O_4 material. Again, 5%Mo has a pore diameter of

20.6 nm, which is close to that of pure Co_3O_4. As shown in **Figure 1(b)**, all the materials

exhibit type IV isotherms followed by type I hysteresis loops indicating the mesoporosity

of the material and the surface area increased from 70 to 96 m^2/g when going from pure

to 3%Mo-Co_3O_4. All materials showed uniform pore size distributions in BJH pore size

analyses except the 5%Mo-Co_3O_4 sample. In that way the 5%Mo-Co_3O_4 material does

not follow the same trend as other materials in consideration. Structural parameters of

each material are summarized in **Table 1**.

We also performed CO_2 adsorption studies using CO_2-BET and the CO_2 adsorption curves for Co_3O_4, 3%Mo-Co_3O_4, and $CoMoO_4$ materials as shown in **Figure 1(d)**. Higher numbers of basic sites provides highly active sites for CO_2 adsorption, hence reducing the capability for adsorption. Despite the lower surface area, undoped Co_3O_4 gave the highest CO_2 adsorption among all three materials. CO_2 adsorption curves for the 3%Mo sample deviated from that of undoped Co_3O_4 significantly to a lower adsorption capacity, which can be ascribed to the fewer basic sites in the 3%Mo material. We checked the CO_2 adsorption for $CoMoO_4$ as a comparison and gave the lowest adsorption among all three materials.

Table 1. Structural parameters of X%Mo-Co_3O_4 catalyst (X=0, 1, 3 and 5)

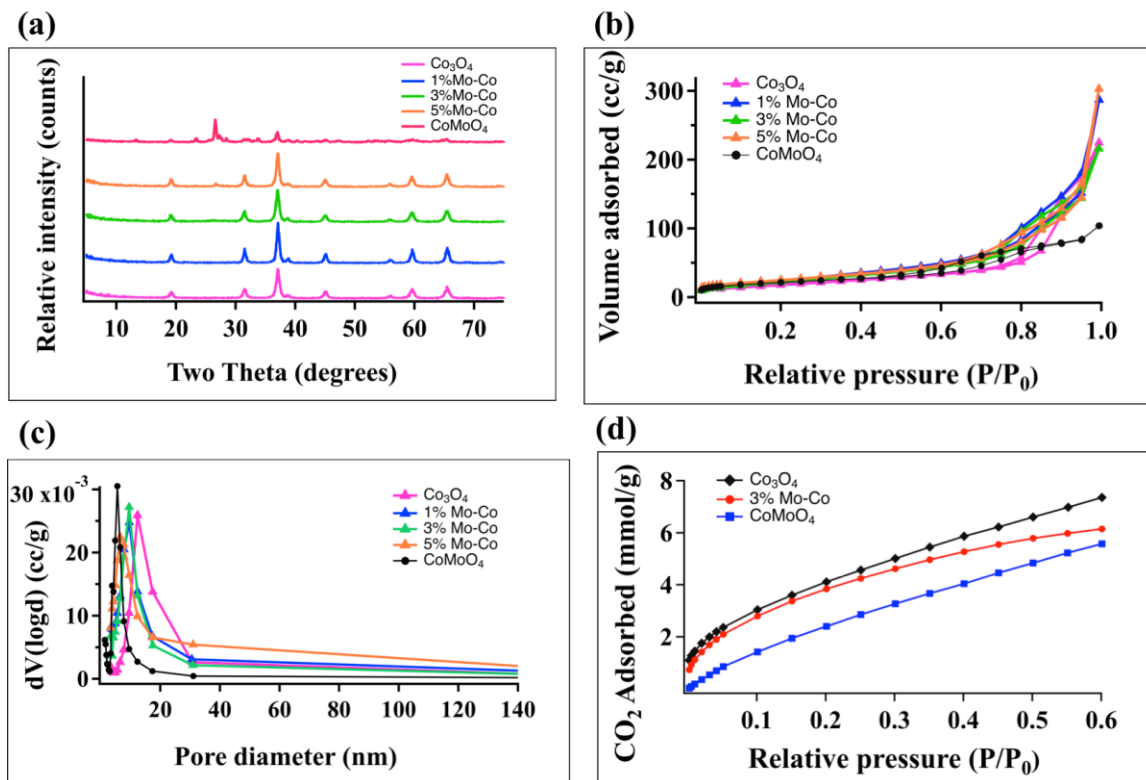| Mo loading %	BET surface area (m^2/g)	BJH Des. pore diameter (nm)	Scherer crystallite size (nm)	d-spacing (nm)
0	70	20.0	14.74	0.242201
1	96	18.5	11.34	0.242529
3	86	15.5	11.20	0.242732
5	91	20.6	13.29	0.242612

Figure 1. Characterization of as-prepared materials: (a) Wide angle XRD patterns, (b) N_2 sorption isotherms, (c) BJH desorption pore size distributions, and (d) CO_2 adsorption curves for X%Mo-Co_3O_4 materials, X=0, 1, 3 and 5
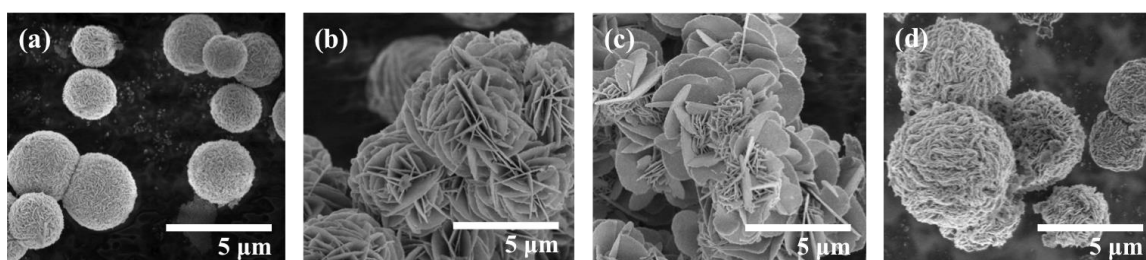

Figure 2. SEM images of (a) Co_3O_4, (b) 1%Mo-Co_3O_4, (c) 3%Mo-Co_3O_4 and (d) 5%Mo-Co_3O_4 materials
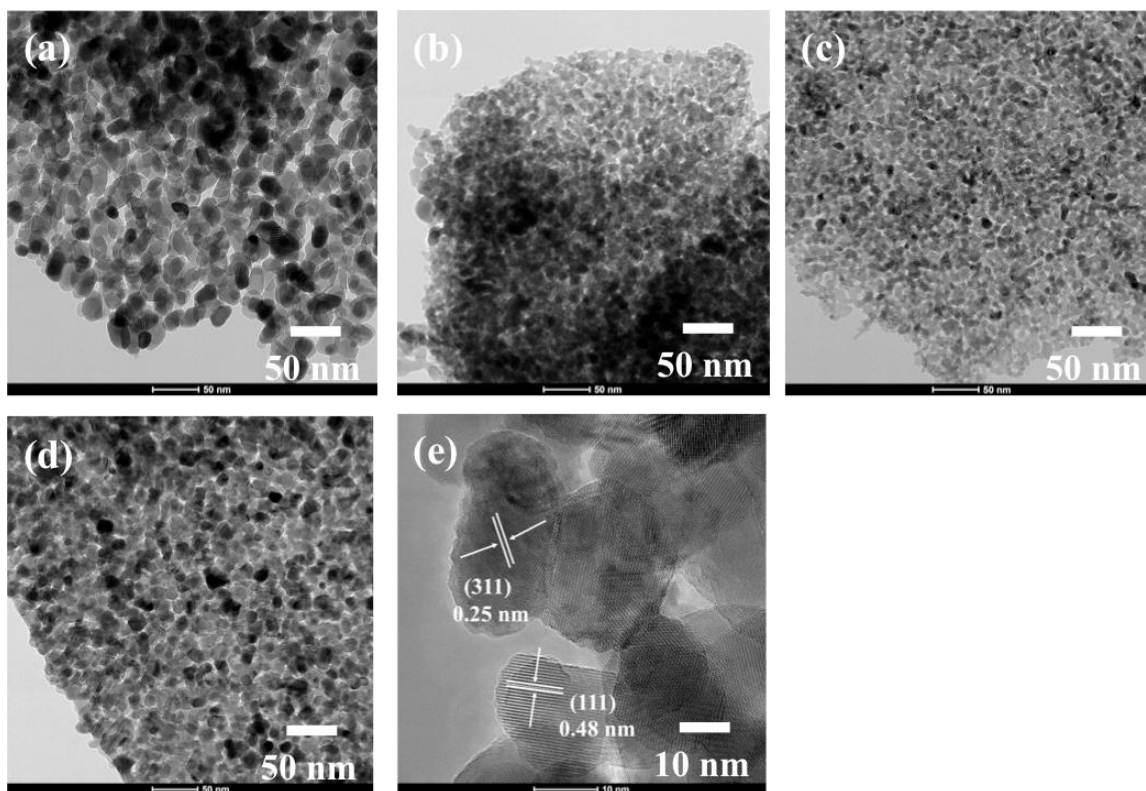
Figure 3. (a-d) TEM images of (a) Co_3O_4, (b) 1%Mo-Co_3O_4, (c) 3%Mo-Co_3O_4 and (d) 5%Mo-Co_3O_4 (e) High magnification TEM of 3%Mo-Co_3O_4

3.1.3. Scanning electron microscopy (SEM) and Energy-dispersive X-ray spectroscopy

(EDX)

Morphological differences in each material could be clearly seen in SEM images given in

Figure 2. Pure Co_3O_4 has spherical particles with rough surfaces and the morphology

gradually changed to flower like structures consisting of nanosize flakes. A homogeneous

distribution of Mo could be observed in EDX mapping for 1% and 3%Mo promoted

samples (**Figure S2**). However, 5%Mo-Co_3O_4 material showed two types of particles,

large round shape particles similar to pure Co_3O_4 along with minor impurity particles

deposited on large particles. These small particles contained Mo/Co in 1:1 ratio according

11

to elemental analyses via EDX mapping. This observation is consistent with PXRD data as we observed peaks for $CoMoO_4$ in 5%Mo-Co_3O_4.

Changes in surface area, pore structure, and morphology of Co_3O_4 suggest successful introduction of Mo into the crystal structure up to 3%Mo concentration. Higher Mo loading did not create significant morphological or structural changes to the original Co_3O_4 structure but formed an additional phase, identified as $CoMoO_4$ mixed metal oxide by PXRD.
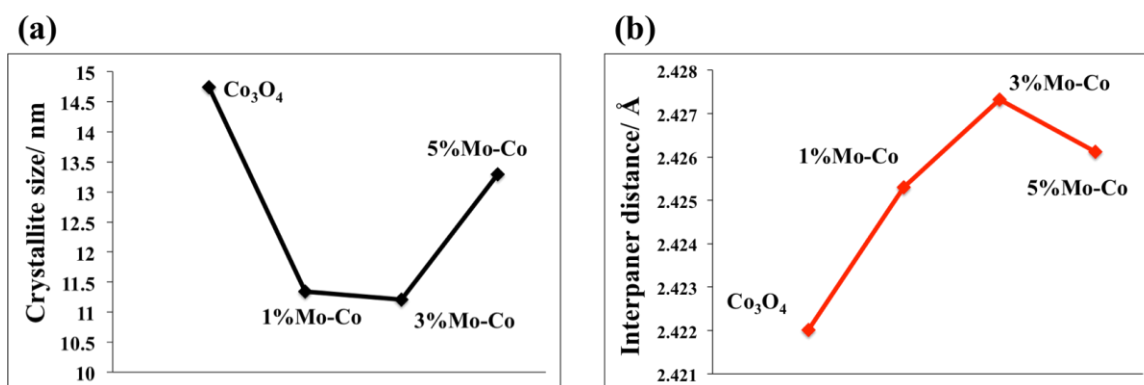
(a)

(b)

Figure 4. Crystallite size and d-spacing values calculated using PXRD data for X%Mo-Co_3O_4 materials, X=0, 1, 3 and 5

3.1.4. Raman spectroscopy

Figure S3 shows the Raman spectra of pure and Mo doped Co_3O_4 nanoparticles. Five Raman bands were identified located at 195, 479, 522, 616, and 686 cm^{-1}. They correspond to A_{1g}, E_g and F_{2g} lattice vibrations of Co^{2+} and Co^{3+} cations situated at tetrahedral and octahedral sites of the cubic Co_3O_4 structure.[24,25] The A_{1g} mode is related to vibrations of octahedral sites and E_g and F_{2g} modes are arising from combined vibrations of tetrahedral sites and octahedral oxygen vibrations.[26] Peak shifts towards

12

higher wave number were observed in 1 and 3% Mo loaded materials. At the same time, increased intensity was observed in Raman peaks with increasing Mo loadings. No peaks were observed for $CoMoO_4$ phase as compared to the Raman spectra of pure $CoMoO_4$ (**Figure S3**).

3.1.5. X-ray photoelectron spectroscopy (XPS)

X-ray photoelectron spectroscopy is a useful technique to study the surface properties and metal valence states of metal oxide materials. Co 2p spectra for 0% to 5%Mo-Co_3O_4 samples are given in **Figure 5(a)**, and Co 2p peaks at binding energies of ~779 and 795 eV are characteristic of Co^{3+}, while the peaks at ~781 and 797 eV correspond to Co^{2+}.[27–29] The Co^{2+}/Co^{3+} ratio was calculated for each sample using areas under the peak in deconvoluted spectra and the values are given in **Table 2**. Bare Co_3O_4 has the highest Co^{3+} percentage of 59% and went down significantly upon Mo insertion where 1%Mo and 3%Mo samples contained 46% and 40% of Co^{3+} respectively. However, 5%Mo material has comparatively higher Co^{3+} amounts of 48%, which is a little lower than pure Co_3O_4, but higher than both the 1% and 3% samples. Similar trends were observed for the lattice oxygen where the Mo introduction decreased lattice oxygen density up to 3% doping concentration. Deconvoluted O 1s spectra in **Figure 5(b)** have two major oxygen contributions, with peaks centered at 529.5 and 531.5 binding energies, which can be attributed to lattice oxygen and surface adsorbed oxygen species, respectively.[23,30] The increased asymmetry to the higher binding energy side of the O 1s peak indicates the increase in adsorbed oxygen species compared to lattice oxygen in turn suggests the formation of more oxygen vacancies.[31] Density of oxygen vacancies increased

13

significantly from 45% to 61% from bare Co_3O_4 to 3%Mo-Co_3O_4. However the 5%Mo material did not fall in the trend with characteristics in between pure Co_3O_4 and 1%Mo materials, which might be due to the incomplete insertion of Mo into the Co_3O_4 lattice. Furthermore XPS data reveal that Mo present in the material is mostly Mo^{6+} and Mo^{5+} can be seen as a minor phase. Deconvoluted Mo 3d spectra for all samples give nearly similar Mo^{6+}/Mo^{5+} ratios, indicating the molybdenum loading amount does not have a significant effect on the oxidation state of Mo in the material.

Table 2. Summary of area percentages of different elemental components obtained from the deconvoluted XPS spectra

Sample	% Area					
	Co 2p $_{3/2}$		O 1s		Mo 3d	
	Co^{3+}	Co^{2+}	O_L	O_V	Mo^{6+}	Mo^{5+}
Co_3O_4	58.6	41.4	55.1	44.9	N/A	N/A
1%Mo-Co_3O_4	45.8	54.2	49.4	50.6	94.7	5.3
3%Mo-Co_3O_4	40.1	59.8	38.9	61.1	90.0	10.0
5%Mo-Co_3O_4	48.5	51.5	49.0	51.0	91.5	8.5
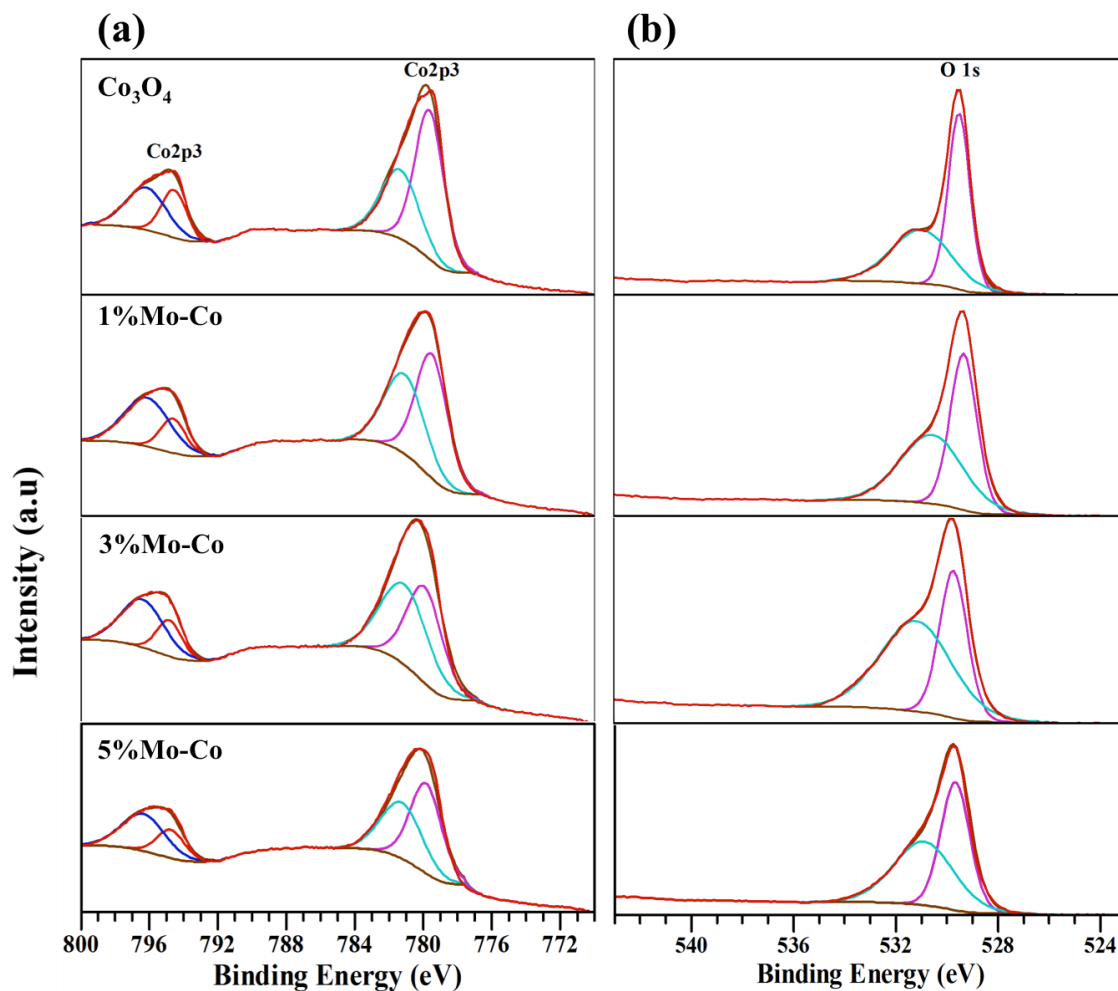
Figure 5. X-ray photoelectron spectroscopy (XPS) analysis: (a) Co 2p and (b) O 1s deconvoluted XPS spectra of Co_3O_4 and X%Mo-Co_3O_4 (X=1,3, and 5)
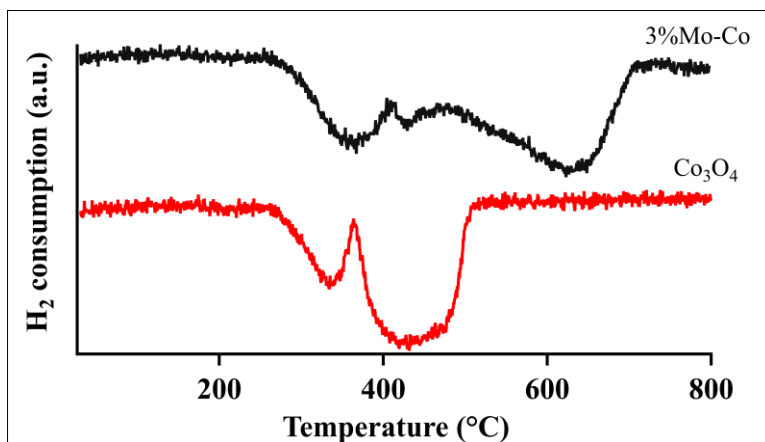
15

Figure 6. H_2-TPR profiles of mesoporous Co_3O_4 and 3%Mo-Co materials. The measurements were conducted from room temperature to 800 °C (10 °C/min) under a stream of 5% H_2/Ar with a flow rate of 50 sccm.

3.2. Catalytic activity evaluation

Liquid phase batch mode reactions of benzylamine with *o*-phenylenediamine were used as model reactions to investigate the structure activity relationships of Mo modified Co_3O_4 catalysts. Reactions were carried out using 1-butanol as the solvent, refluxed under air at 100 °C and with no additives. Conversion and selectivity of each catalyst were investigated for the two possible products, which are 2-substituted benzimidazole (1a) and 1,2-disubstituted benzimidazole (1b). Apparently, the control experiment with no catalysts did not form any products for this reaction. Bare Co_3O_4 gave 45% conversion after three hours and the product (1a) selectivity was 72%. Interestingly, within 3 hours 3%Mo-Co_3O_4 catalyst showed enhanced product selectivity of 96% and a conversion of 58%. When the reaction time increased to 5 hours, 100% conversion was achieved with 97% selectivity. However, the selectivity dropped by 17% when 5%Mo-Co_3O_4 was used as the catalyst. The 5%Mo sample contains $CoMoO_4$ as an impurity phase in the material.

16

Thus, pure $CoMoO_4$ was used as the catalyst under similar reaction conditions. $CoMoO_4$ showed high selectivity (67%) for 1,2-disubtituted benzimidazole, which was not the product of interest. 3%Mo-Co catalyst was recycled and reused, and the second reuse cycle gave 90% conversion with 92 % selectivity.
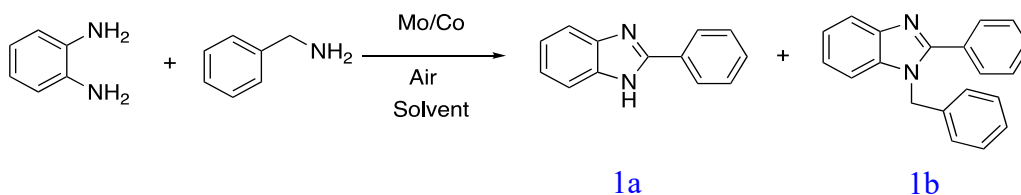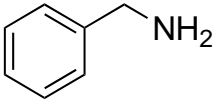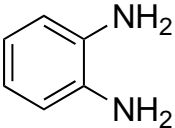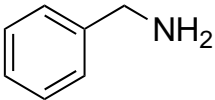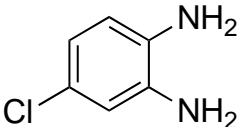

Table 3. Conversion and selectivity of X%Mo-Co_3O_4 and $CoMoO_4$ catalysts for benzimidazole synthesis reaction
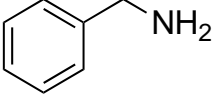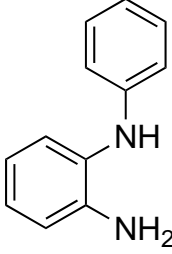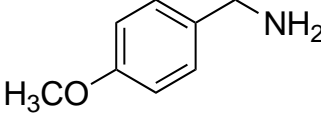
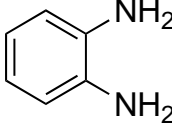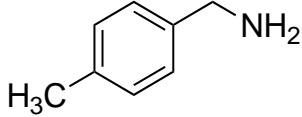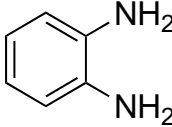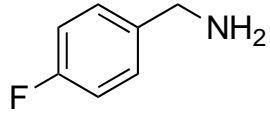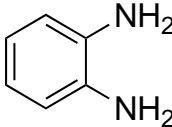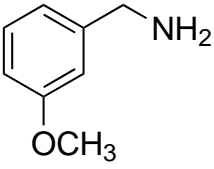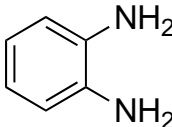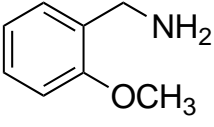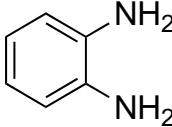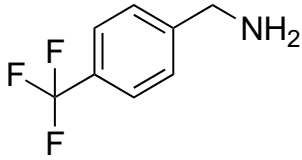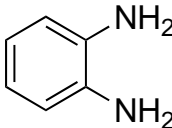| Catalyst	Time/h	Conversion %	Selectivity	
			1a	1b
No catalyst	3	0	NA	NA
Co_3O_4	3	45	72	28
1%Mo-Co_3O_4	3	50	84	16
3%Mo-Co_3O_4	3	58	96	4
5%Mo-Co_3O_4	3	55	79	21
$CoMoO_4$	3	30	33	67
3%Mo-Co_3O_4	5	100	97	3
3%Mo-Co_3O_4[a]	5	90	92	8

Reaction conditions: Catalyst 10 mg, Butanol 1ml, 100 °C, o-phenylenediamine 0.5 mM, benzylamine 0.6 mM, reflux under air, Conversions were determined by GC-MS based on the concentration of o-phenylenediamine. [a] Recycled catalyst.

The 3%Mo-Co$_3$O$_4$ material was identified as the best catalyst for the selective synthesis of 1-substituted product and was selected as the catalyst for further studies. To investigate the versatility of the catalyst towards a variety of substrates, a series of different starting materials were subjected to similar reaction conditions and the conversions and selectivities were calculated for the 1-substituted product.

Table 4. Catalytic activity of 3%Mo-Co$_3$O$_4$ catalyst for the reaction of different substituted benzylamine and diamine towards 1-substituted benzimidazole synthesis

Entry	Benzyl amine	Diamine	% Conversion	% Selectivity
1			100	97
2			60	67

No.	Substrate	Diamine	Conversion	Yield
3	benzylamine	2-anilinoaniline (NH, NH₂)	100	90
4	4-methoxybenzylamine	o-phenylenediamine	95	93
5	4-methylbenzylamine	o-phenylenediamine	92	82
6	4-fluorobenzylamine	o-phenylenediamine	85	62
7	3-methoxybenzylamine	o-phenylenediamine	63	62
8	2-methoxybenzylamine	o-phenylenediamine	70	83
9	4-(trifluoromethyl)benzylamine	o-phenylenediamine	93	76

Reaction conditions: Catalyst 10 mg, Butanol 1ml, 100 °C, diamine 0.5 mM, substituted benzylamine 0.6 mM, reflux under air, 5h. Conversions were determined by GC-MS based on the concentration of o-phenylenediamine

19

3.3. Reaction mechanism and kinetics

The high catalytic activity and selectivity of Mo-Co$_3$O$_4$ towards the desired reaction motivated us for the investigation of mechanistic details. Trace amounts of benzaldehye were found to be present in the initial stage of reaction mixture according to the GC-MS results. To further evaluate the fate of benzylamine in the reaction mixture when there is no diamine present, a separate experiment was carried out with only benzylamine as the starting reagent and Mo-Co$_3$O$_4$ as the catalyst. The major product obtained was the corresponding imine with trace amounts of benzaldehyde. In this reaction pathway, the first step is aldehyde formation, which then reacts with another molecule of amine to give imine.[32] No imine product was observed, indicating the reaction of benzaldehyde with diamine happens at a faster rate compared to benzylamine, in the presence of diamine in the reaction mixture. **Scheme 1** gives the suggested reaction mechanism for the formation of benzaldehyde from benzylamine where H$^+$ abstraction is the rate determining step.[32] The generation of the benzylamine radial intermediate caused the reduction of Co^{3+} to Co^{2+} on the catalyst surface, which led to the facile release of labile lattice oxygen.[33,34] Lattice oxygen combines with the protons (H$^+$) and electrons released from metal ion reduction to form water.

20
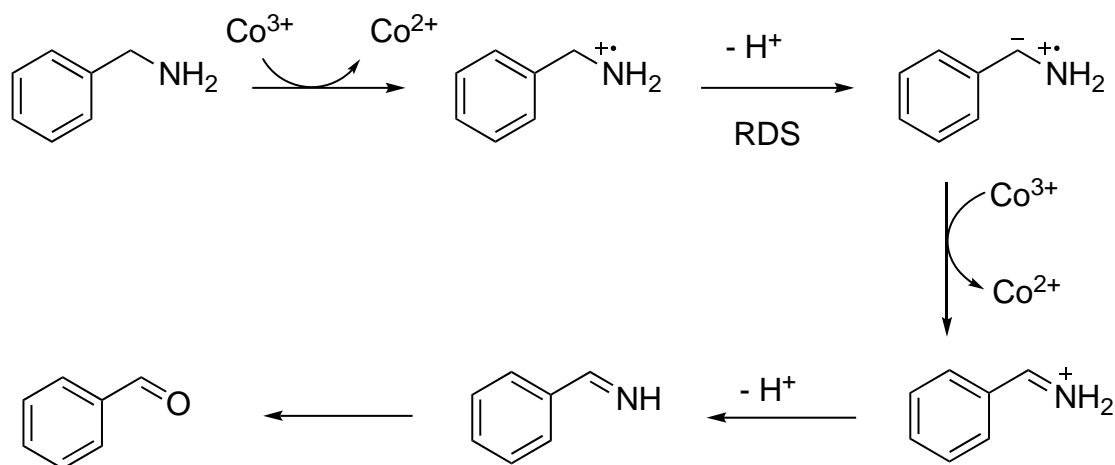
Scheme 1. Reaction pathway of oxidation of benzylamine to benzaldehyde

The surface acidity of the catalyst has a considerable effect on determining the rate of formation of benzaldehyde as proton abstraction is the rate determining step in the given reaction pathway (**Scheme 1**). Basic sites on the catalyst surface could enhance the rate by promoting H^+ abstraction, thereby generating the aldehyde at a higher rate. For instance, Cs promoted MnO_x catalyst has been employed for amine to imine conversion and showed remarkable enhancement in catalytic activity compared to bare MnO_x.[32] Here, Cs incorporation was identified as the factor to increase the basic sites of the metal oxide material, which in turn helps to improve the conversion efficiency of amine to imine.

Mo doping in Co_3O_4 catalyst has an influential effect on the selectivity of the product formation between 1-substituted and 1,2-substituted benzimidazole. CO_2 adsorption data show an enhancement of surface acidity when Mo was incorporated into the Co_3O_4 crystal lattice. Therefore, to determine the relationship between surface acidity of the

21

catalyst and rate of formation of benzaldehyde, two sets of kinetic data were collected using bare Co_3O_4 and $3\%Mo\text{-}Co_3O_4$ as the catalyst (**Figure 7**).
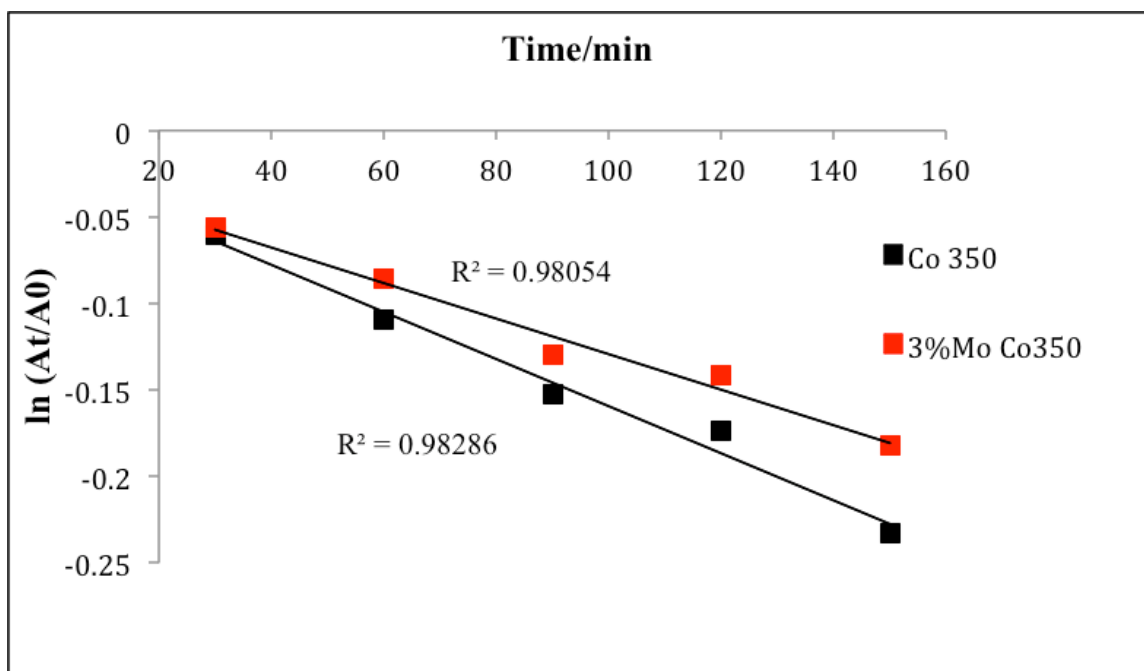

Figure 7. Kinetic plots for the oxidation of benzylamine catalyzed by Co_3O_4 and $3\%Mo\text{-}Co_3O_4$

A proposed reaction mechanism for the dehydrogenative coupling of aromatic diamine and aldehyde is given in **Scheme 2**. Oxidation of amine produces aldehyde, which then couples with the diamine, forming a Schiff base imine intermediate **2** by water elimination. This will then be subjected to cyclization to produce 2-phenyl-2,3-dihydro-1H-benzimidazole, which rapidly dehydrogenates to form the corresponding 1-substituted benzimidazole product, **4**.[35] However, a higher rate of production of aldehyde will lead to formation of diimine intermediate **5**, which subsequently converts to 1,2-disubstituted benzimidazole derivative.
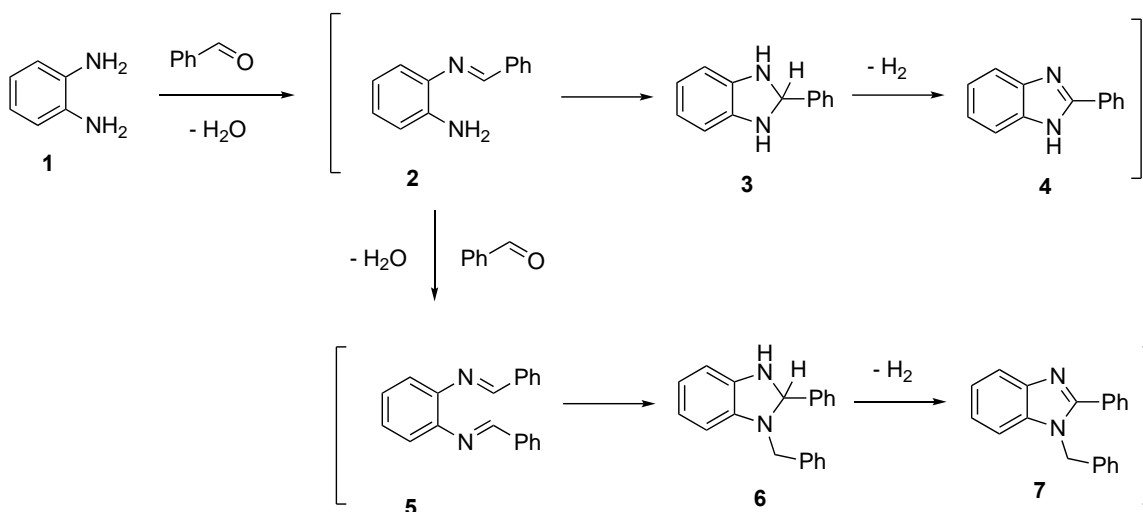
Scheme 2. Plausible steps involved in benzimidazole synthesis from 1,2 diaminobenzene and benzaldehyde, catalyzed by Mo-Co$_3$O$_4$ catalyst

Kinetic data reveal that bare Co$_3$O$_4$ produces benzaldehyde at a higher rate compared to Mo-Co$_3$O$_4$, when used as the catalyst. This is in good agreement with the observed product selectivity with two catalysts, where the catalyst with more acidic character, shows high selectivity towards 2-disubstituted benzimidazoles.

4. Discussion

With regard to sustainable synthesis, an environmentally benign pathway for the synthesis of benzimidazoles with high product selectivity would be highly desirable. Bi-functional nature of the cobalt catalyst in terms of basicity and dehydrogenative properties could be considered as major contributions for more proficient benzimidazole synthesis.[35] However, acid/base and redox properties of the catalyst are the key factors to

23

determine the product selectivity of benzimidazole synthesis reactions. In this work we demonstrate molybdenum introduction into the Co_3O_4 lattice, which has a great influence on creating acidic sites and oxygen vacancies in the material. Reduced CO_2 adsorption by Mo-Co_3O_4 material compared to bare Co_3O_4 (**Figure 1(d))** indicates that the number of acidic sites has been increased upon Mo addition. Successful incorporation of Mo into the Co_3O_4 lattice could be observed up to 3%Mo loading concentration. When the Mo addition increased to 5% molar concentration, formation of $CoMoO_4$ mixed metal oxide was identified as a separate phase. According to the XPS data, molybdenum was mainly found in its 6+ oxidation state. The Co^{3+}/Co^{2+} ratio decreased significantly with the increased Mo concentration implying that Mo^{6+} substitutes for Co^{3+} in the Co_3O_4 crystal lattice (**Table 2**). This would enhance the formation of oxygen vacancies on the catalyst surface due to charge compensation, which in turn is responsible for the formation of surface defects that can act as active sites for the adsorption and activation of reactant molecules.[36,37] XPS data shows significant increase in surface oxygen vacancy density of the CO_3O_4 material upon molybdenum addition. Increased oxygen vacancy density indicates the enhancement of the surface acidic character of the material.[38] Reduced basicity of the catalyst, control the rate of formation of benzaldehyde facilitating the selective formation of 2-benzimidazole according to the reaction pathway shown in **Scheme 2.**

Catalysts with higher activity toward oxidation reactions generally have higher reducibility.[39] H_2-TPR measurements were performed to compare the redox properties of molybdenum promoted and pure cobalt oxides (**Figure 6**). The reducibility of Co_3O_4 is highly dependent on the dispersion state of particles, thus large particles are usually

24

reduced to metallic cobalt in a single step while nanoparticles goes through a two step reduction process.[23] The reduction behavior of pure cobalt oxide starts with a sharp peak around 350 °C, which can be attributed to the reduction of Co^{3+} to Co^{2+} ($Co_3O_4 \rightarrow CoO$), followed by a broad peak in the range of 400-500 °C corresponding the reduction of CoO to metallic Co. In the H_2-TPR profile of Mo-Co_3O_4, both reduction peaks shifted to higher temperatures, indicating the lower reducibility of the material compared to pure Co_3O_4.

Strain caused by the large density of oxygen defects creates a lattice expansion and therefore, nanocrystallites preferentially grow in the direction of (311) planes.[40,41] D-spacings calculated using Bragg's law indicate the variation of inter-planar distances upon Mo incorporation (**Figure 4**). Scherrer crystallite sizes were found to be decreasing with increasing $d_{(311)}$, implying a reciprocal relationship with crystallite size and d spacing.[42,43] Stronger and sharper Raman peaks were observed for Mo-Co_3O_4 and the peaks slightly shifted to a higher wave number. This effect can be attributed to the particle size enhancement in Mo-Co_3O_4, as the Raman peak intensity is dependent on the grain size of the material.[44] Doping molybdenum produced Raman peak shifts to a higher energy compared to that of pure Co_3O_4, as a result of lattice deformation.[45]

Catalysts reported for benzimidazole synthesis have both acidic and basic sites. Thus, acidic strength of the catalyst is an important factor in directing the product selectivity.[35,46,47] Therefore, careful adjustment of acid/base nature would promote the synthesis of a new catalytic material with enhanced activity for selective organic transformations. Molybdenum incorporation makes the material more acidic and the amount of Mo^{6+} in the lattice determines the strength of acidity in each catalyst.

25

Having analyzed the optimum reaction conditions for 2-phenylbenzimidazole, the substrate scope and limitations were explored for different types of amine substrates. Many substituents on the phenyl group of benzylamine, such as p-Me, p-OMe, m-Cl, p-Cl, were tolerant to the oxidative cyclization (**Table 4**). Different 1,2-diaminobenzene derivatives were also tested under similar reaction conditions. Electron donating or electron withdrawing groups on the aromatic ring of 1,2-diaminobenzenes were well tolerated under these cyclization reaction conditions, and the desired benzimidazoles were obtained in good yields.

Enhanced surface characteristics of the modified catalyst, showed a remarkable effect on the selective synthesis of 2-phenylbenzimidazole. This reaction is likely to follow the pathway of coordination of Schiff bases (imine intermediate, **2**) onto the acid sites of the catalyst, followed by cyclization and dehydrogenation to give desired product as shown in **Scheme 2**.[47] Stabilization of intermediate **2** (Schiff base), by the acidic sites of the catalyst, hinders the reaction of a second molecule of aldehyde with the imine intermediate, thereby inhibiting the formation of disubstituted product. Combined effects of acid-base strength, O_2 vacancy density, and surface defects play a major role in controlling the product selectivity in the above-mentioned reaction mechanism. Overall, careful modification of mesoporous cobalt oxide catalyst by introducing molybdenum in minor quantities has been recognized as a tool to develop a unique catalytic material for selective synthesis of benzimidazoles.

5. Conclusion

In conclusion, a one-pot, highly selective, and efficient catalytic protocol has been

26

developed for the synthesis of 2-substituted benzimidazoles. Catalytic activity of Co_3O_4 has been improved by introducing molybdenum as an impurity into the lattice structure, where Mo^{6+} replaces the Co^{3+} in the crystal lattice, which alters the surface oxygen vacancies, surface defects, and redox properties of the original material. The reaction is applicable to a wide range of diamine and benzylamine substrates with excellent yields. A plausible mechanism is proposed. This developed synthesis protocol provides an attractive pathway for selective benzimidazole production, being environmentally benign, and cost effective, using an earth-abundant metal, and forming H_2O and H_2 as the sole byproducts.

Acknowledgement

Keywords: Lattice expansion, Mesoporous materials, Molybdenum substitution, Surface oxygen vacancies, 2-Substituted benzimidazoles.

References
1   J. Wan, S. Gan, J. Wu and Y. Pan, *Green Chem.*, 2009, **11**, 1633–1637.
2   Z. H. Zhang, L. Yin and Y. M. Wang, *Catal. Commun.*, 2007, **8**, 1126–1131.

27

3   R. J. Perry and B. D. Wilson, *J. Org. Chem.*, 1993, **58**, 7016–7021.

4   C. T. Brain and S. A. Brunton, *Tetrahedron Lett.*, 2002, **43**, 1893–1895.

5   M. P. Surpur, P. R. Singh, S. B. Patil and S. D. Samant, *Synth. Commun.*, 2007, **37**, 1375–1379.

6   L. M. Dudd, E. Venardou, E. Garcia-Verdugo, P. Licence, A. J. Blake, C. Wilson and M. Poliakoff, *Green Chem.*, 2003, **5**, 187–192.

7   F. Rajabi, S. De and R. Luque, *Catal. Letters*, 2015, **145**, 1566–1570.

8   Z. Xu, D. Wang, X. Yu and Y. Yang, *Adv. Synth. Catal.*, 2017, **359**, 3332–3340.

9   T. Hille, T. Irrgang and R. Kempe, *Chem. A Eurpean J.*, 2014, **20**, 5569–5572.

10 R. Ramachandran, G. Prakash, S. Selvamurugan, P. Viswanathamurthi, J. G. Malecki and V. Ramkumar, *Dalt. Trans.*, 2014, **43**, 7889–7902.

11 K. D. Parghi and R. V. Jayaram, *Catal. Commun.*, 2010, **11**, 1205–1210.

12 S. B. Rathod, M. K. Lande and B. R. Arbad, *Bull. Korean Chem. Soc.*, 2010, **31**, 2835–2840.

13 J. Dawody, M. Skoglundh and E. Fridell, *J. Mater. Sci. Lett.*, 2004, **209**, 215–225.

14 E. C. Tyo, C. Yin, M. Di Vece, Q. Qian, G. Kwon, S. Lee, B. Lee, J. E. Debartolo, S. Seifert, R. E. Winans, R. Si, B. Ricks, S. Goergen, M. Rutter, B. Zugic, M. Flytzani-Stephanopoulos, Z. W. Wang, R. E. Palmer, M. Neurock and S. Vajda, *ACS Catal.*, 2012, **2**, 2409–2423.

15 I. Bauer, H. Kn, C. À. H. Bond, F. Cross and C. Arylalkylation, *Chem. Rev.*, 2015, **115**, 3170–3387.

16 P. J. Chirik, *Acc. Chem. Res.*, 2015, **48**, 1687–1695.

17 A. Mukherjee, A. Nerush, G. Leitus, L. J. W. Shimon, Y. Ben David, N. Angel, E. Jalapa and D. Milstein, *J. Am. Chem. Soc.*, 2016, **138**, 4298–4301.

18 S. Chakraborty, P. Bhattacharya, H. Dai and H. Guan, *Acc. Chem. Res.*, 2015, **48**, 1995–2003.

19 W. Song, Z. Ren, S. Y. Chen, Y. Meng, S. Biswas, P. Nandi, H. A. Elsen, P. X. Gao and S. L. Suib, *ACS Appl. Mater. Interfaces*, 2016, **8**, 20802–20813.

20 N. D. Wasalathanthri, A. S. Poyraz, S. Biswas, Y. Meng, C. H. Kuo, D. A. Kriz and S. L. Suib, *J. Phys. Chem. C*, 2015, **119**, 1473–1482.

21 C. Weerakkody, S. Biswas, W. Song, J. He, N. Wasalathanthri, S. Dissanayake, D. A. Kriz, B. Dutta and S. L. Suib, *Appl. Catal. B Environ.*, 2018, **221**, 681–690.

22 A. S. Poyraz, C.-H. Kuo, S. Biswas, C. K. King'ondu and S. L. Suib, *Nat. Commun.*, 2013, **4**, 2952.

23 W. Song, A. S. Poyraz, Y. Meng, Z. Ren, S. Y. Chen and S. L. Suib, *Chem. Mater.*, 2014, **26**, 4629–4639.

24 B. S. Yeo and A. T. Bell, *J. Am. Chem. Soc.*, 2011, **133**, 5587–5593.

25 B. Rivas-murias, *J. Raman Spectrosc.*, 2017, **48**, 837–841.

26 J. Yang, H. Liu, W. N. Martens and R. L. Frost, *J. Phys. Chem. C*, 2010, **114**, 111–119.

27 Z. Ren, Y. Guo, Z. Zhang, C. Liu and P.-X. Gao, *J. Mater. Chem. A*, 2013, **1**, 9897.

28 Y. Ding, L. Zhu, A. Huang and X. Zhao, *Catal. Sci. Technol.*, 2012, **2**, 1977–1984.

29 M. C. Biesinger, B. P. Payne, A. P. Grosvenor, L. W. M. Lau, A. R. Gerson, R. St and C. Smart, *Appl. Surf. Sci.*, 2011, **257**, 2717–2730.

30 P. Zhang, X. Li, Q. Zhao and S. Liu, *Nanoscale Resech Lett.*, 2011, **6**, 323–330.

31   M. J. Jackman, A. G. Thomas and C. Muryn, *J. Phys. Chem. C*, 2015, **119**, 13682–13690.

32   S. Biswas, B. Dutta, K. Mullick, C.-H. Kuo, A. S. Poyraz and S. L. Suib, *ACS Catal.*, 2015, **5**, 4394–4403.

33   V. D. Makwana, Y.-C. Son, A. R. Howell and S. L. Suib, *J. Catal.*, 2002, **210**, 46–52.

34   A. Grirrane, A. Corma and H. Garcia, *Science (80-.).*, 2008, **322**, 1661–1665.

35   P. Daw, Y. Ben-David and D. Milstein, *ACS Catal.*, 2017, **7**, 7456–7460.

36   X. Liu and B. Shan, *Catal. Sci. Technol.*, 2017, **7**, 4462–4469.

37   L. Wang, Y. Yu, H. He, Y. Zhang, X. Qin and B. Wang, *Sci. Rep.*, 2017, 12845.

38   C. Mrabet, N. Mahdhi, A. Boukhachem, M. Amlouk and T. Manoubi, *J. Alloys Compd.*, 2016, **688**, 122–132.

39   W. Shan, W. Shen and C. Li, *Chem. Mater.*, 2003, **88**, 4761–4767.

40   B. Santara, P. K. Giri, K. Imakita and M. Fujii, *J. Phys. D. Appl. Phys.*, 2014, **47**, 215302.

41   J. Sheng, U. Welzel, E. J. Mittemeijer, J. Sheng, U. Welzel and E. J. Mittemeijer, *Appl. Phys. Lett.*, 2010, **97**, 153109.

42   C. R. Aita, M. C. Cisneros-morales and E. E. Hoppe, *J. Phys. Chem. C*, 2012, **116**, 26679–26680.

43   R. Banerjee, E. A. Sperling, G. B. Thompson, H. L. Fraser, S. Bose, P. Ayyub, R. Banerjee, E. A. Sperling, G. B. Thompson and H. L. Fraser, *Appl. Phusics Lett.*, 2003, **82**, 4250–4252.

44   C. Stella, N. Soundararajan, K. Ramachandran, C. Stella, N. Soundararajan and K. Ramachandran, *AIP Adv.*, 2016, **87104**, 87104–87114.

45   A. Jha, D. Jeong, Y. Lee, I. W. Nah and H. Roh, *RSC Adv.*, 2015, **5**, 103023–103029.

46   A. Teimouri, A. Najafi, H. Salavati and L. Ghorbanian, *J. Mol. Catal. A. Chem.*, 2013, **373**, 38–45.

47   A. Teimouri and A. N. Chermahini, *J. Mol. Catal. A Chem.*, 2011, **346**, 39–45.

29